


Topological phase transition in Sb-doped Mg₃Bi₂ monocrystalline thin filmsTong Zhou ^{1,2,3,4} Mingyu Tong,⁵ Yun Zhang,^{1,4} Xiangnan Xie,² Zhen-Yu Wang,^{2,6,7,*} Tian Jiang,^{2,3,†} Xie-Gang Zhu,^{1,4,‡} and Xin-Chun Lai¹¹Science and Technology on Surface Physics and Chemistry Laboratory, Jiangyou 621908, Sichuan, People's Republic of China²State Key Laboratory of High Performance Computing, College of Computer,

National University of Defense Technology, Changsha 410073, People's Republic of China

³Beijing Institute for Advanced Study, National University of Defense Technology, Beijing 100020, People's Republic of China⁴Institute of Materials, China Academy of Engineering Physics, Mianyang 621700, Sichuan, People's Republic of China⁵College of Advanced Interdisciplinary Studies, National University of Defense Technology, Changsha 410073, People's Republic of China⁶National Innovation Institute of Defense Technology, Academy of Military Sciences PLA China, Beijing 100010, People's Republic of China⁷Beijing Academy of Quantum Information Sciences, Beijing 100193, People's Republic of China

(Received 10 October 2020; accepted 19 February 2021; published 3 March 2021)

Mg₃Bi₂ has been proved to be a semimetal with topological surface states (referred to as a topological semimetal, TSM) in the presence of spin-orbit coupling (SOC), and predicted to be a type-II nodal line semimetal (NSM) in the absence of SOC. It is possible to tune the effective SOC in Mg₃Bi₂ by substituting the heavy Bi atom with lighter atoms, such as Sb or As, which results in topological phase transitions. Here in our work we investigate the evolution of the transport properties and band structures of Mg₃Bi₂ by doping different concentrations of Sb through molecular beam epitaxy. Our results demonstrate the existence of phase transitions of TSM to trivial semimetal (SM) and SM to trivial insulator, with Sb concentration x at $x_1 \approx 0.44$ – 0.64 and $x_2 \approx 1.39$, respectively. Further theoretical calculations give values of $x_1 \approx 0.523$ and $x_2 \approx 1.10$, which agrees well with our experimental results. And all these results are concluded into a Mg₃Bi_{2-x}Sb_x phase diagram. Our work will stimulate more explorations to the possibilities of the realization of type-II NSM in Mg₃Bi₂ by various elements substitution.

DOI: [10.1103/PhysRevB.103.125405](https://doi.org/10.1103/PhysRevB.103.125405)**I. INTRODUCTION**

Band engineering aims to control the electronic structures of materials by different methods to adjust their physical properties and/or to achieve certain artificial functions [1–5]. These methods include manipulating the dimensionality, tuning the chemical composition (such as doping), proximity to different materials, etc. For topological materials, their topological properties are embodied in the characteristics of their electronic structures [6–8]. Upon doping an appropriate dopant, their electronic structures, such as band gap or spin-orbit coupling (SOC), could be continuously tuned, which would result in topological phase transitions [9–12].

Mg₃Bi₂ is predicted as a type-II nodal line semimetal without SOC, and its nodal line loop will open a gap of about 35 meV in the presence of the SOC effect [13,14], resulting in a semimetal with topological surface states, similar to antimony that is a semimetal and possesses topological surface states. Hereafter we define a semimetal with topological surface states as a topological semimetal, abbreviated as TSM. As aforementioned, doping is an effective way to control SOC. Therefore, it is worth doping Mg₃Bi₂ with another element to manipulate its topological properties. Among

the candidate elements in the periodic table, Sb is a priority option [4,15], in the sense that (1) Sb and Bi belong to the same family in the periodic table, and they could alloy with each other to form Bi_{1-x}Sb_x alloys with an arbitrary Bi/Sb chemical ratio, while the rhombohedral lattice structure is preserved. (2) Mg₃Bi₂ is a TSM, while Mg₃Sb₂ is a trivial insulator. The alloying of the two materials could most probably result in topological phase transitions. (3) Due to the weaker SOC of Sb, Sb doping could realize a reduced effective SOC strength in Mg₃Bi_{2-x}Sb_x, and a type-II NSM is expected.

In this work Mg₃Bi_{2-x}Sb_x single crystalline films with different Sb doping concentration (x) were grown on graphene/6H-SiC(0001) and Al₂O₃ substrates by molecular beam epitaxy (MBE). *In situ* reflection high-energy electron diffraction (RHEED) and *ex situ* x-ray diffraction (XRD) were performed on Mg₃Bi_{2-x}Sb_x films to demonstrate the evolution of lattice structure. Magnetotransport were also carried out to study the transport properties of Mg₃Bi_{2-x}Sb_x. The band structures were characterized by *in situ* angle resolved photoemission spectroscopy (ARPES) measurements. Based on the above experimental results, a substitution phase diagram was illustrated. In this phase diagram we have identified that Mg₃Bi_{2-x}Sb_x is a TSM with $x < 0.44$, a trivial SM with $x > 0.64$, and a trivial insulator with $x > 1.39$. Theoretical calculations were performed to simulate the above phase transitions, and the results agree very well with our experimental results.

*oscarwang2008@sina.com

†tjiang@nudt.edu.cn

‡zhuxiegang@caep.cn

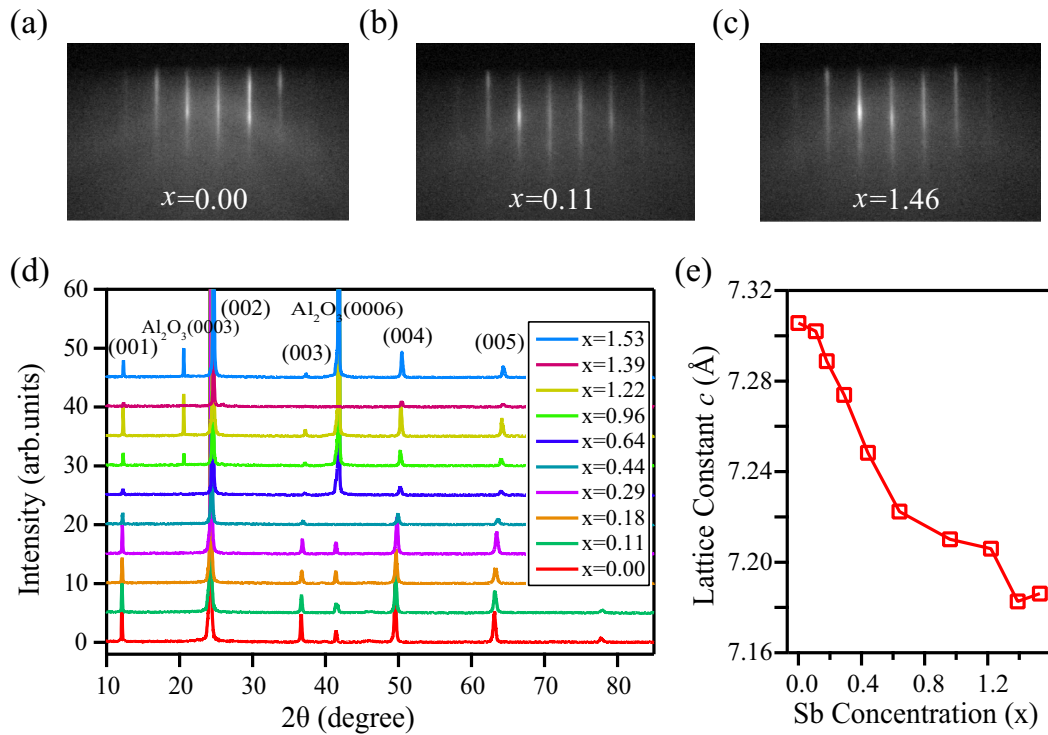


FIG. 1. Characteristics of $\text{Mg}_3\text{Bi}_{2-x}\text{Sb}_x$ thin films on Al_2O_3 by RHEED and XRD. (a), (b), and (c) RHEED patterns of Mg_3Bi_2 , Mg_3Bi_2 , $\text{Mg}_3\text{Bi}_{1.89}\text{Sb}_{0.11}$, and $\text{Mg}_3\text{Bi}_{0.54}\text{Sb}_{1.46}$, respectively. (d) The XRD spectra of $\text{Mg}_3\text{Bi}_{2-x}\text{Sb}_x$ with various Sb concentration. The spectra are vertically offset for clarity. (e) The summary of *out-of-plane* lattice constant c with various Sb concentration.

II. METHODS

Mg, Bi, and Sb were evaporated from independent Knudsen cells to grown $\text{Mg}_3\text{Bi}_{2-x}\text{Sb}_x$ films. The concentration x is calibrated from the temperature and vapor pressure of Bi and Sb sources [16,17], based on the relationship between vapor pressure and rate of evaporation in a vacuum [18]. The thickness of the samples is about 100 nm. And the films for XRD and transport experiments were grown on $\text{Al}_2\text{O}_3(0001)$ substrates, while substrates of single-layer graphene epitaxially grown on 6H-SiC(0001) were used for the ARPES experiments. The transport measurements were performed with the standard four-probe technique using a physical property measurement system (PPMS-9). Silver electrodes were connected to the sample surface with indium contact, and transport measurements were performed above the onset superconducting transition temperature of indium, i.e., 3.4 K, to eliminate the influence of the superconducting indium on the transport properties. For the photoemission spectroscopy experiment, the spectra were excited by the $\text{He I}\alpha$ (21.2 eV) resonance line of a commercial helium gas discharge lamp. The light is guided to the analysis chamber by a quartz capillary. In virtue of the efficient four-stage differential pumping system, the pressure in the analysis chamber is better than 1.0×10^{-10} mbar during our experiments. A VG Scienta R4000 energy analyzer is used to collect the photoelectrons.

The DFT calculations were performed by using the VASP code with the projector augmented-wave (PAW) approach to core-valence interactions. HSE06 hybridized density functional approximation was used to improve the accuracy in the calculations of energy gaps. The Brillouin zone is

sampled with $11 \times 11 \times 7$ Γ -centered k mesh for self-consistent calculations. SOC effect is fully taken into consideration throughout the whole calculations. The VASP2WANNIER90 interface is used to construct the first-principles tight-binding Hamiltonian. Mg s and p and Bi/Sb p orbitals are taken into consideration and no maximizing localization procedure is performed to construct the Wannier orbitals [19–21]. Since doping calculation is a challenge in DFT, in order to theoretically locate the critical point for the phase transition in $\text{Mg}_3\text{Bi}_{2-x}\text{Sb}_x$, we linearly hybridized the tight-binding Hamiltonians for Mg_3Bi_2 and Mg_3Sb_2 to present the Hamiltonians of $\text{Mg}_3\text{Bi}_{2-x}\text{Sb}_x$ with arbitrary Sb concentration, and make use of the WANNIERTOOLS packages [22] to calculate the corresponding electronic structures.

III. RESULTS AND DISCUSSIONS

A. Lattice structure of $\text{Mg}_3\text{Bi}_{2-x}\text{Sb}_x$ thin films

The *in-plane* lattice constant of Mg_3Bi_2 is 4.675 Å [14], while that of $\text{Al}_2\text{O}_3(0001)$ is 4.758 Å. There is only a 1.7% mismatch between them, which makes $\text{Al}_2\text{O}_3(0001)$ a good substrate for the epitaxial growth of $\text{Mg}_3\text{Bi}_{2-x}\text{Sb}_x$ thin films. The films were preliminarily characterized by *in situ* RHEED and *ex situ* XRD. Figures 1(a)–1(c) display the RHEED patterns of Mg_3Bi_2 , $\text{Mg}_3\text{Bi}_{1.89}\text{Sb}_{0.11}$, and $\text{Mg}_3\text{Bi}_{0.54}\text{Sb}_{1.46}$. The sharp RHEED streaks demonstrate the high quality of our *as-grown* $\text{Mg}_3\text{Bi}_{2-x}\text{Sb}_x$ films with arbitrary Sb concentration. This can be contributed to the fact that Mg_3Bi_2 and Mg_3Sb_2 are in the same type of lattice and their lattice constants are

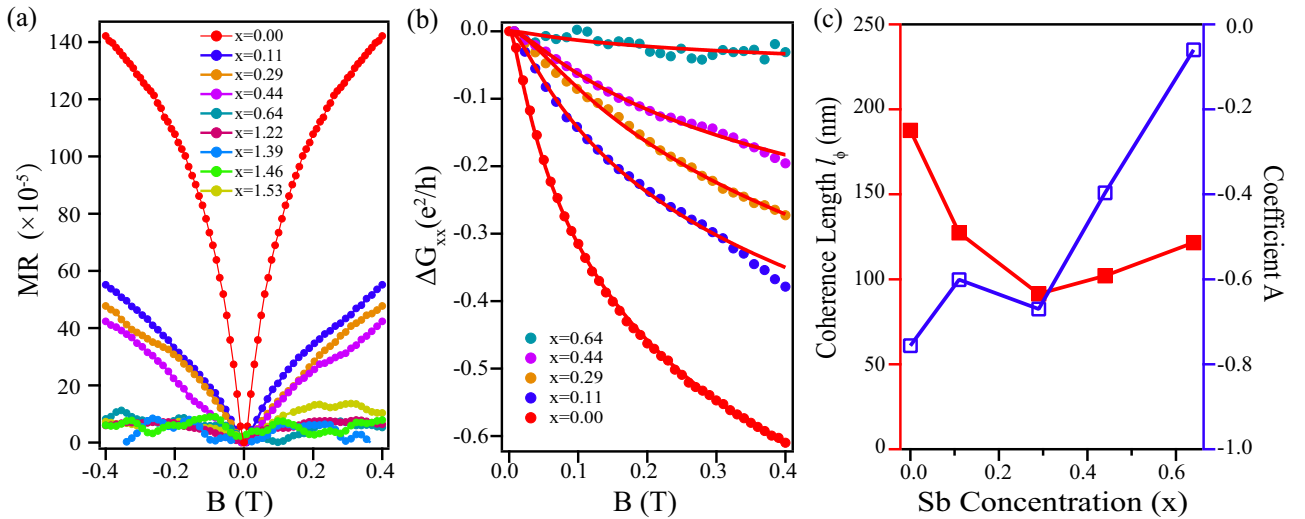


FIG. 2. WAL effects in $\text{Mg}_3\text{Bi}_{2-x}\text{Sb}_x$ films. (a) The magnetoresistance of $\text{Mg}_3\text{Bi}_{2-x}\text{Sb}_x$ films with different x . When $x < 0.44$, there are dip features near the zero magnetic field for the magnetoresistance curves. When $x > 0.64$, the dip disappears. (b) Magnetoconductance in perpendicular magnetic field configuration measured for different Sb concentration samples and their best fits to the HLN equation. (c) The extracted coherence length l_ϕ (left-hand axis) and coefficient A (right-hand axis) from the HLN fitting under different x .

very close. Doping Sb atoms did not introduce any destructive disturbance in the original lattice structure of Mg_3Bi_2 . As for the XRD results, it can be seen in Fig. 1(d) that XRD spectra clearly present $(001n)$ peaks of $\text{Mg}_3\text{Bi}_{2-x}\text{Sb}_x$. Furthermore, these peaks gradually right shifted as the Sb concentration increases. The *out-of-plane* lattice constant c can be calculated from XRD spectra and the results with various Sb concentration are summarized in Fig. 1(e). With the increase of Sb concentration, c monotonically decreases from 7.307 Å at $x = 0.00$ to 7.171 Å at $x = 1.46$, which is consistent with the value of Mg_3Bi_2 ($c = 7.416$ Å) and Mg_3Sb_2 ($c = 7.243$ Å) as reported in previous works. Therefore, our RHEED and XRD results confirmed MBE as an effective method for doping Sb in Mg_3Bi_2 and also revealed the high crystalline quality and the evolution of lattice structure of our $\text{Mg}_3\text{Bi}_{2-x}\text{Sb}_x$ films.

B. Transport properties

Transport measurements were performed on $\text{Mg}_3\text{Bi}_{2-x}\text{Sb}_x$ films grown on $\text{Al}_2\text{O}_3(0001)$ substrate. We aimed to explore the magnetoresistance, resistivity, and carrier behavior evolution for samples with various Sb concentrations. Figure 2(a) presents magnetoresistance of $\text{Mg}_3\text{Bi}_{2-x}\text{Sb}_x$ with the resistance measured at 3.5 K. The magnetoresistance is defined as $MR = \frac{R(B) - R(0)}{R(0)}$, where $R(B)$ and $R(0)$ are the resistances measured under magnetic field of B and zero field, respectively. When the Sb concentration x is lower than 0.44, the magnetoresistance curves showed a dip behavior near zero magnetic field, which demonstrates the well-known weak antilocalization (WAL) effects. WAL is a quantum interference effect. WAL enhances the conductivity with decreasing temperature due to the destructive quantum interference of two closed electrons scattering paths [23]. Our previous work reports that this WAL effect originates from the topological bands of Mg_3Bi_2 [24,25]. As the Sb concentration x increased to 0.44–0.64, the dip vanished, indicating the absence of the

topological bands. Or in other words, this means the existence of topological phase transition from topological semimetal to trivial semimetal. WAL is an important phenomenon that reflects critical transportation properties of a system, such as symmetry, phase coherence length, number of conducting channels, and so on [23,26,27]. The three-dimensional (3D) nodal line model [25] is not that sensitive to the gap of its nodal ring, which is the exact factor that is tuned by doping Sb. To quantitatively analyze the WAL effect evolution, we fitted our experiment data by the Hikami-Larkin-Nagaoka (HLN) model [24,28] which focuses on the two-dimensional (2D) topological surface states (TSS). HLN formula is commonly used to fit the correction magnetoconductivity caused by WAL effects. The model was derived in a 2D system with random potential scattering while considering the SOC effects. Besides the 2D system, it is also suitable for the conducting 2D TSS in a 3D insulator [23,29,30]. The HLN formula reads

$$\Delta G_{xx}(B) \equiv G(B) - G(0) \cong A \frac{e^2}{2\pi^2\hbar} \left[\Psi \left(\frac{1}{2} + \frac{B_\phi}{B} \right) - \ln \left(\frac{B_\phi}{B} \right) \right],$$

where $G(B)$ is the magnetoconductivity, A is the coefficient of WAL, e is the element electron charge, \hbar is the reduced Planck constant, Ψ is the Digamma function, $B_\phi = \hbar/(4el_\phi^2)$ is the characteristic magnetic field, and l_ϕ is the phase coherence length.

Figure 2(b) represents the magnetoconductivity variation of $\text{Mg}_3\text{Bi}_{2-x}\text{Sb}_x$ film (dotted line) and their best fitting results (solid lines) to the HLN model. The fitted phase coherence length l_ϕ and coefficient A are demonstrated in Fig. 2(c). The coefficient $A = N\alpha$, where α is -0.5 and N means the number of conducting channels. As shown in Fig. 2(c), A varies from -0.76 to -0.06 , as Sb concentration x increases from 0.00 to 0.64. This indicates the topological conducting channel is closed due to the increasing Sb concentration or the

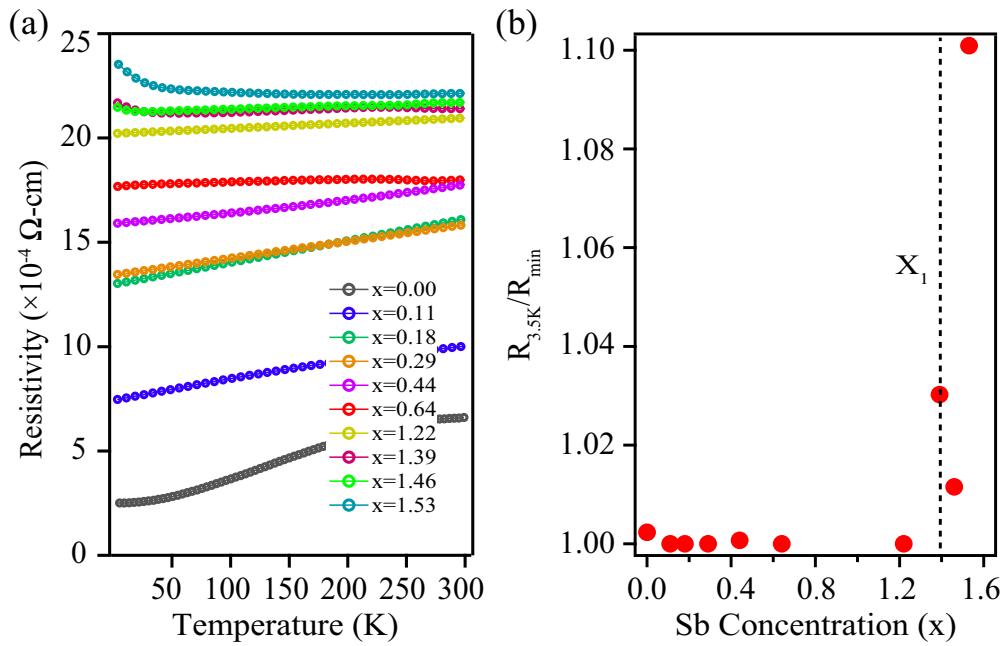


FIG. 3. Transport measurement on Mg₃Bi_{2-x}Sb_x. (a) The temperature dependence of longitudinal resistivity of Mg₃Bi_{2-x}Sb_x films with various values of x . (b) $R_{3.5\text{K}}/R_{\min}$ vs x , exhibiting a metal/semimetal to insulator transition at around $x = 1.39$.

dissolving of the topological bands in Mg₃Bi_{2-x}Sb_x. Therefore, by quantitatively analyzing the WAL effects, specifically, the topological conducting channel from the WAL coefficient A , we confirmed that there is a topological to trivial phase transition when Sb concentration is between $x = 0.44$ to $x = 0.64$. More importantly, we also established the evolution of the WAL effect as a topological phase transition evidence, in a system where the WAL effect originates from the topological bands.

The temperature dependence of longitudinal resistivity ρ_{xx} on Sb concentration x is shown in Fig. 3(a). The measured temperature increases from 3.5 to 300 K. As shown in Fig. 3(a), as the Sb concentration increases, ρ_{xx} gradually increases. Besides, when $x < 1.39$, the resistivity keeps decreasing as the temperature decreases, demonstrating the tendency of metal/semimetal behavior, which indicates that the electron-phonon scattering dominated the resistivity. When $x > 1.39$, the resistivity turns upward as the temperature decreases, which means that Mg₃Bi_{2-x}Sb_x is no longer a metal/semimetal but an insulator. Therefore, the evolution of $R(T)$ curves show how the system changes from a metallic/semimetallic state to an insulator state as x increases [9]. We also plotted $R_{3.5\text{K}}/R_{\min}$ vs x in Fig. 3(b), in which the transition from a metal/semimetal to insulator at $x = 1.39$ could be clearly figured out. Although the value of $R_{3.5\text{K}}/R_{\min}$ at $x = 1.46$ is smaller than that of $x = 1.39$, which may be caused by the measurements or contacts factors, the upward trend is consistent.

C. ARPES experiments

We further performed ARPES measurements on Mg₃Bi_{2-x}Sb_x films on single-layer graphene which is epitaxially grown from SiC substrate. The growth condition is

similar to that of the films grown on Al₂O₃. Figures 4(a)–4(f) present the band structure in the \bar{K} - $\bar{\Gamma}$ - \bar{K} direction for thin films with different Sb concentration. Previous experimental ARPES results and theoretical calculation results have shown that the topological surface states and the energy where the nodal line is expected to appear could be found in literature [14] and also in the Supplemental Material [31]. Sb doping did not induce fundamental changes to the main features of the band structures, except the gradual shift of all the band structures away from the Fermi level. To quantitatively evaluate the shift of bands structures, we have extracted the dispersions of S bands from the momentum distribution curves (EDCs) of ARPES spectra, and fitted them with parabolic line shape, as shown in Fig. 4(g). The Fermi crossing points of the fitted bands were summarized in Fig. 4(h), in which the shift of the band structures was well demonstrated. Although Mg₃Bi₂ is theoretically topological semimetal, in reality it showed conducting behavior with heavy p -type carrier [32]. The case for Mg₃Sb₂ is similar, i.e., it is a semiconductor in theory and was p -type experimentally [32,33]. Our transport experiments showed that the Hall carriers for all the Mg₃Bi_{2-x}Sb_x samples were p type, and their density decreased with increasing Sb concentration, which equivalently meant the increasing of electron doping and resulted in the downwards shift of the band structures. What is more, the shift of the band structures decreases rapidly as x increases from 0.00 to 0.73, and tends to vary a little as x further increases, which is consistent with the variation of the carrier density.

The shifting behaviors cause the gap near the Fermi level to emerge and be extended, and finally cause the system to evolve into an insulator phase. Therefore, by ARPES measurements, the evolution of Mg₃Bi_{2-x}Sb_x band structure is observed, and the transition from a semimetal

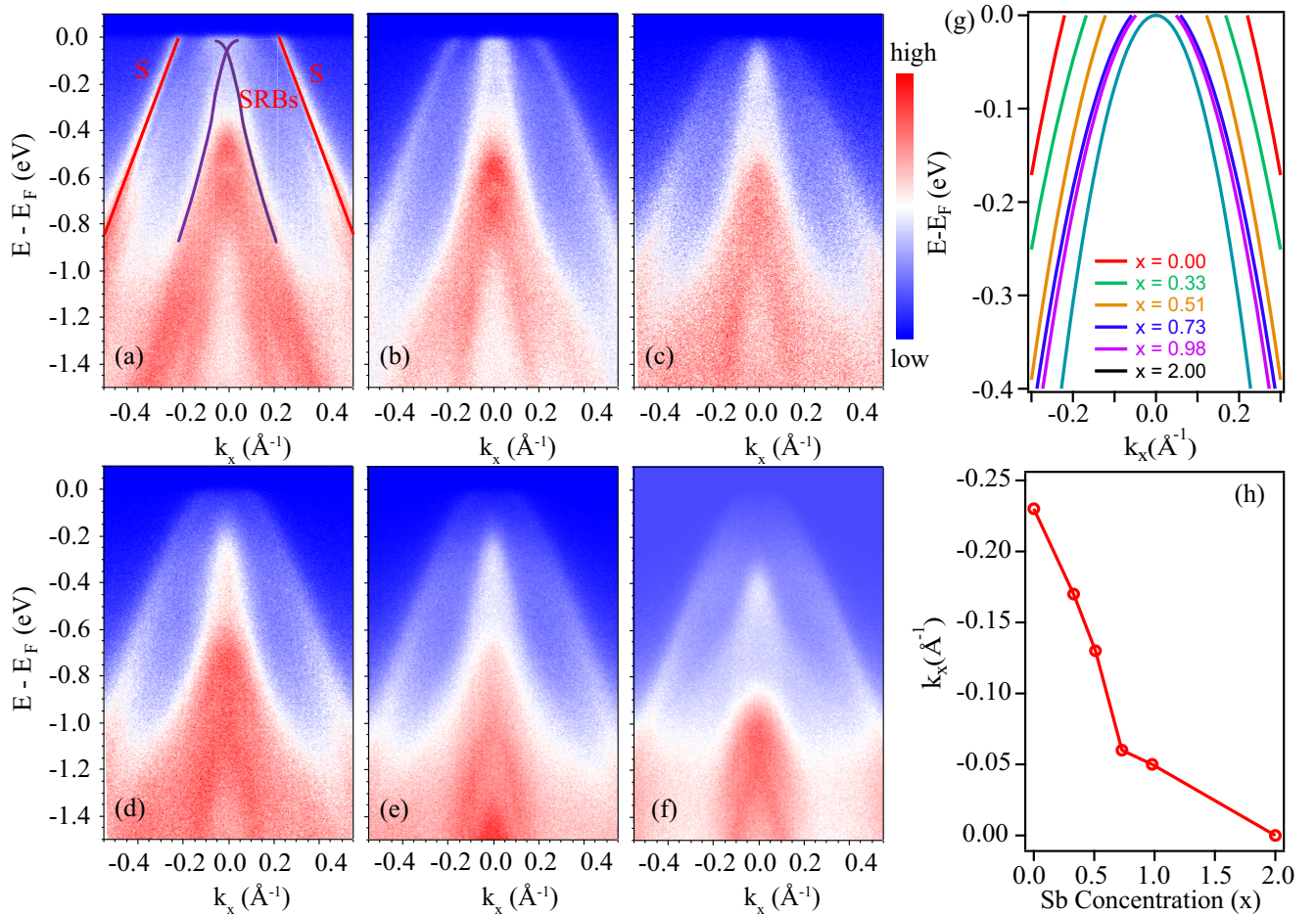


FIG. 4. Band structure evolution of $\text{Mg}_3\text{Bi}_{2-x}\text{Sb}_x$ measured by ARPES. (a)–(f) $\text{Mg}_3\text{Bi}_{2-x}\text{Sb}_x$ band structure with Sb concentration at $x = 0.00$, $x = 0.33$, $x = 0.51$, $x = 0.73$, $x = 0.98$, and $x = 2.00$. As the Sb concentration increases, the band undergoes two changes: (1) S band shifts gradually and breaks away from Fermi level and (2) SRB band shifts and also breaks away from Fermi level. (g) and (h) The fitting of S bands for samples with different Sb concentration and the Fermi crossing points of the fitted bands.

phase (Mg_3Bi_2) into an insulator phase (Mg_3Sb_2) is vividly presented.

D. Theoretical calculations

The electronic structures of Mg_3Bi_2 and Mg_3Sb_2 have already been theoretically studied [13,14,24,34], which showed the topological nature of Mg_3Bi_2 and the trivial insulator nature of Mg_3Sb_2 . Even for $\text{Mg}_3\text{Bi}_{2-x}\text{Sb}_x$ alloys, DFT calculations based on supercell structures have been systematically carried out [35]. However, theoretically, the topological phase transitions in $\text{Mg}_3\text{Bi}_{2-x}\text{Sb}_x$, as the Sb concentration x varies from 0 to 2, were not properly taken into consideration in those previous studies. Due to the limitations of DFT calculations for alloying with arbitrary Sb concentration, it is almost impossible to determine the critical points for the phase transitions in $\text{Mg}_3\text{Bi}_{2-x}\text{Sb}_x$. We avoided this issue by using the tight-binding methods. As the lattice constants (a and c) of Mg_3Bi_2 and Mg_3Sb_2 differ by a factor less than 2.5% [34], we have used the same calculation parameters (lattice structures, control parameters for the calculation softwares, etc., except the pseudopotentials for Bi and Sb elements) during

the DFT calculation and wannierization procedures for the two materials, which guarantee the same structure of the two resultant Hamiltonians. The tight-binding Hamiltonians for Mg_3Bi_2 and Mg_3Sb_2 were linearly hybridized to represent the Hamiltonian of $\text{Mg}_3\text{Bi}_{2-x}\text{Sb}_x$, similar to the way in dealing with $\text{Bi}_{1-x}\text{Sb}_x$ alloys [36–38].

The bulk band structures reconstructed from the above-mentioned tight-binding Hamiltonians for Mg_3Bi_2 and Mg_3Sb_2 along high symmetric k path in the bulk Brillouin zone are shown in Figs. 5(a) and 5(b), respectively, which are consistent with the results from the literature [13,14]. Mg_3Sb_2 is a trivial insulator with an indirect energy gap of 340 meV, while Mg_3Bi_2 is a topological semimetal with a 350 meV energy overlapping of the valence and conduction bands near Fermi level. (The detailed information about the energy gap and overlapping of Mg_3Sb_2 and Mg_3Bi_2 could be found in the Supplemental Material [31].) As for $\text{Mg}_3\text{Bi}_{2-x}\text{Sb}_x$, band structures along M - Γ - K were calculated for a series of x values, as shown in Figs. 5(c)–5(f). To investigate the potential phase transitions, it is straightforward to evaluate the evolution of the energy gap. Here we take the conventional definition of a negative energy gap for topological insulators

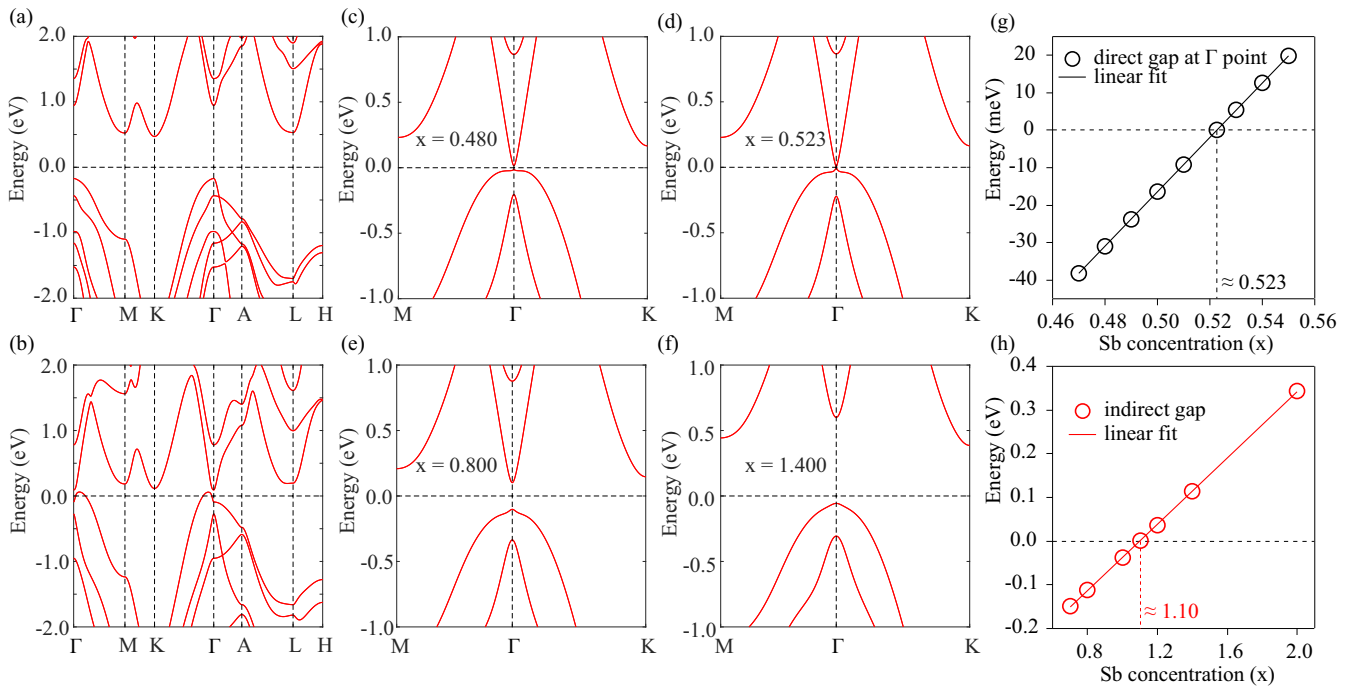


FIG. 5. Theoretical calculation results of the band structure evolution of $\text{Mg}_3\text{Bi}_{2-x}\text{Sb}_x$. (a) and (b) Bulk band structures which are reconstructed from tight-binding Hamiltonians for Mg_3Sb_2 and Mg_3Bi_2 , respectively. (c)–(f) Band structures of $\text{Mg}_3\text{Bi}_{2-x}\text{Sb}_x$ along M - Γ - K for $x = 0.480$, 0.523 , 0.800 , and 1.400 , respectively. (f) Evolution of the direct gap at Γ near the topological semimetal to trivial semimetal phase transition. (g) Evolution of the indirect gap for the topological semimetal to trivial semimetal phase transition.

as a result of band inversion. We noticed that a band inversion did happen in $\text{Mg}_3\text{Bi}_{2-x}\text{Sb}_x$ as Sb concentration x increased, i.e., the negative band gap at Γ slowly closed and re-opened as x went across the critical value of 0.523 , as shown in Fig. 5(g). The calculated scattered data sets of energy gap versus x could be nicely fitted by a straight line, which is due to the linear hybridization of the two Hamiltonians for Mg_3Bi_2 and Mg_3Sb_2 . The above crossover indicates the topological semimetal to trivial semimetal phase transition. Once again we define the indirect gap as negative for the trivial semimetal phase, in the sense that the valence and conduction bands overlap each other. As x keeps on increasing, the indirect gap experiences a crossover from negative to positive near 1.10 , where the phase transition from trivial semimetal to trivial insulator happens, as shown in Fig. 5(h). It should be noted that the zero energy in Figs. 5(c)–5(f) was set at the center of the direct negative energy gap for the semimetal phases, while at the center of the indirect positive energy gap for the insulating phase. We can see that the calculated x value for the topological semimetal to trivial semimetal (≈ 0.523) matches well with the estimated experimental value (0.44 – 0.64), and that for the trivial semimetal to insulator (≈ 1.10) is also comparable to the experimental value of ~ 1.39 from transport experiments.

Our calculations have revealed the existence of the phase transitions of the topological semimetal to trivial semimetal and trivial semimetal to trivial insulator in $\text{Mg}_3\text{Bi}_{2-x}\text{Sb}_x$ as x varies from 0 to 2 . It was expected that a phase transition from topological semimetal to nodal-line semimetal might happen in Mg_3Bi_2 , in the case that the heavy element Bi was replaced by lighter elements, such as Sb or As. Based on our

calculations, this did not happen in Sb doping. Doping Bi by Sb only induces the transition from topological semimetal to trivial semimetal, and then to trivial insulator. However, As

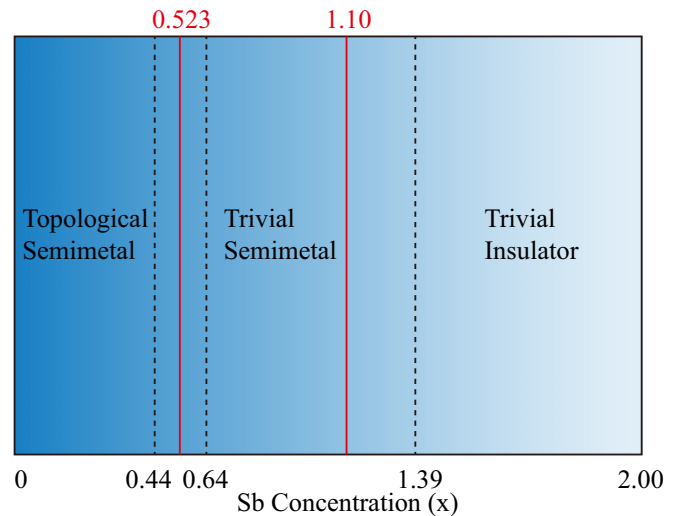


FIG. 6. $\text{Mg}_3\text{Bi}_{2-x}\text{Sb}_x$ phase diagram with various Sb concentration x resulting from the experiments (black dotted line) and theoretical calculations (red solid line). With the increasing doping of Sb, $\text{Mg}_3\text{Bi}_{2-x}\text{Sb}_x$ experiences topological semimetal, trivial semimetal, and finally trivial insulator phases. The experiments localized the critical values of x lay on 0.44 – 0.64 and 1.39 for the topological-to-trivial semimetal and trivial semimetal-to-insulator transitions, while those values were 0.523 and 1.10 for theoretical calculations.

doping is still worth trying theoretically and experimentally, as As is even lighter than Sb, which might make the phase transition from topological semimetal to nodal-line semimetal possible.

IV. CONCLUSIONS

The phase diagram of $\text{Mg}_3\text{Bi}_{2-x}\text{Sb}_x$ films is concluded in Fig. 6 in which the transition points are demonstrated by a black dotted line and a red solid line from the experimental and the theoretical results, respectively. With the increasing doping of Sb, $\text{Mg}_3\text{Bi}_{2-x}\text{Sb}_x$ experiences topological semimetal, trivial semimetal, and finally trivial insulator phases. As for the topological semimetal to trivial semimetal transition, the experimental and theoretical results confirmed that the critical values of x were 0.44–0.64 and 0.523, in which the results were consistent with each other. However, there was slightly difference between the experiments and theoretical calculations as for the trivial semimetal to trivial insulator transition, which were separately corresponding to

1.39 and 1.1. This difference may caused by the coarsely localizing of the transition point by the experiments which were judged through the change of resistivity trends.

In summary, we have grown single crystalline $\text{Mg}_3\text{Bi}_{2-x}\text{Sb}_x$ thin films with high quality by MBE. The evolution of the electronic structures of $\text{Mg}_3\text{Bi}_{2-x}\text{Sb}_x$ as x varies from 0 to 2 was studied by transport measurements, ARPES experiments, and theoretical calculations. Our investigation results and the processing approaches will broaden the knowledge of $\text{Mg}_3\text{Bi}_{2-x}\text{Sb}_x$ itself and also inspire more explorations on using transport properties, specifically WAL effects, and theoretical calculations to search for novel topological phase transitions.

ACKNOWLEDGMENTS

We thank Quansheng Wu for helpful discussions. This work was supported by the SPC-Lab Research Fund (No. WDZC201901), the BAQIS Research Program Y18G17, and the National Natural Science Foundation of China (Grant No. 12004434).

-
- [1] K.-h. Jin, H. W. Yeom, and S.-h. Jhi, *Phys. Rev. B* **93**, 075308 (2016).
- [2] M. Kang, B. Kim, S. H. Ryu, S. W. Jung, J. Kim, L. Moreschini, C. Jozwiak, E. Rotenberg, A. Bostwick, and K. S. Kim, *Nano Lett.* **17**, 1610 (2017).
- [3] A. N. Andriotis and M. Menon, *J. Appl. Phys.* **117**, 125708 (2015).
- [4] K. Imasato, S. D. Kang, S. Ohno, and G. J. Snyder, *Mater. Horizons* **5**, 59 (2018).
- [5] X. Qian, L. Fu, and J. Li, *Nano Res.* **8**, 967 (2015).
- [6] M. Z. Hasan and C. L. Kane, *Rev. Mod. Phys.* **82**, 3045 (2010).
- [7] Y. Xia, D. Qian, D. Hsieh, L. Wray, A. Pal, H. Lin, A. Bansil, D. Grauer, Y. S. Hor, R. J. Cava, and M. Z. Hasan, *Nat. Phys.* **5**, 398 (2009).
- [8] S.-Y. Xu, C. Liu, S. K. Kushwaha, R. Sankar, J. W. Krizan, I. Belopolski, M. Neupane, G. Bian, N. Alidoust, T.-R. Chang, H.-T. Jeng, C.-Y. Huang, W.-F. Tsai, H. Lin, P. P. Shibaev, F.-C. Chou, R. J. Cava, and M. Z. Hasan, *Science* **347**, 294 (2015).
- [9] M. Brahlek, N. Bansal, N. Koirala, S. Y. Xu, M. Neupane, C. Liu, M. Z. Hasan, and S. Oh, *Phys. Rev. Lett.* **109**, 186403 (2012).
- [10] L. Wu, M. Brahlek, R. V. Aguilar, A. V. Stier, C. M. Morris, Y. Lubashevsky, L. S. Bilbro, N. Bansal, S. Oh, and N. P. Armitage, *Nat. Phys.* **9**, 410 (2013).
- [11] M. Salehi, H. Shapourian, N. Koirala, M. J. Brahlek, J. Moon, and S. Oh, *Nano Lett.* **16**, 5528 (2016).
- [12] Z. Wang, T. Zhou, T. Jiang, H. Sun, Y. Zang, Y. Gong, J. Zhang, M. Tong, X. Xie, Q. Liu, C. Chen, K. He, and Q.-K. Xue, *Nano Lett.* **19**, 4627 (2019).
- [13] X. Zhang, L. Jin, X. Dai, and G. Liu, *J. Phys. Chem. Lett.* **8**, 4814 (2017).
- [14] T.-R. Chang, I. Pletikoscic, T. Kong, G. Bian, A. Huang, J. Denlinger, S. K. Kushwaha, B. Sinkovic, H.-T. Jeng, T. Valla, W. Xie, and R. J. Cava, *Adv. Sci.* **6**, 1800897 (2019).
- [15] J. Zhang and B. B. Iversen, *J. Appl. Phys.* **126**, 085104 (2019).
- [16] A. T. Aldred and J. N. Pratt, *J. Chem. Phys.* **38**, 1085 (1963).
- [17] G. M. Rosenblatt and C. E. Birchenall, *J. Chem. Phys.* **35**, 788 (1961).
- [18] I. Langmuir, *Phys. Rev.* **2**, 329 (1913).
- [19] N. Marzari and D. Vanderbilt, *Phys. Rev. B* **56**, 12847 (1997).
- [20] I. Souza, N. Marzari, and D. Vanderbilt, *Phys. Rev. B* **65**, 035109 (2001).
- [21] A. A. Mostofi, J. R. Yates, Y.-S. Lee, I. Souza, D. Vanderbilt, and N. Marzari, *Comput. Phys. Commun.* **178**, 685 (2008).
- [22] Q. Wu, S. Zhang, H.-F. Song, M. Troyer, and A. A. Soluyanov, *Comput. Phys. Commun.* **224**, 405 (2018).
- [23] H.-Z. Lu and S.-Q. Shen, *Phys. Rev. B* **84**, 125138 (2011).
- [24] T. Zhou, X.-G. Zhu, M. Tong, Y. Zhang, X.-B. Luo, X. Xie, W. Feng, Q. Chen, S. Tan, Z.-Y. Wang, T. Jiang, Y. Tang, X.-C. Lai, and X. Yang, *Chin. Phys. Lett.* **36**, 117303 (2019).
- [25] T. Zhou, M. Tong, X. Xie, Y. Yu, X. Zhu, Z.-Y. Wang, and T. Jiang, *J. Phys. Chem. Lett.* **11**, 6475 (2020).
- [26] H. Z. Lu and S. Q. Shen, *Chin. Phys. B* **25**, 117202 (2016).
- [27] H. Z. Lu and S. Q. Shen, *Phys. Rev. Lett.* **112**, 146601 (2014).
- [28] S. Hikami, A. I. Larkin, and Y. Nagaoka, *Prog. Theor. Phys.* **63**, 707 (1980).
- [29] Y. S. Kim, M. Brahlek, N. Bansal, E. Edrey, G. A. Kapilevich, K. Iida, M. Tanimura, Y. Horibe, S.-W. Cheong, and S. Oh, *Phys. Rev. B* **84**, 073109 (2011).
- [30] W. J. Wang, K. H. Gao, and Z. Q. Li, *Sci. Rep.* **6**, 1 (2016).
- [31] See Supplemental Material at <http://link.aps.org/supplemental/10.1103/PhysRevB.103.125405> for more detailed nodal line and gap opening w/o SOC, spectral function calculations, energy gap and overlapping, and slab versus spectral function calculations.
- [32] J. Xin, G. Li, G. Auffermann, H. Borrmann, W. Schnelle, J. Gooth, X. Zhao, T. Zhu, C. Felser, and C. Fu, *Mater. Today Phys.* **7**, 61 (2018).

- [33] H. Tamaki, H. K. Sato, and T. Kanno, *Adv. Mater.* **28**, 10182 (2016).
- [34] L. M. Watson, C. A. W. Marshall, and C. P. Cardoso, *J. Phys. F* **14**, 113 (1984).
- [35] J. Zhang, L. Song, S. H. Pedersen, H. Yin, L. T. Hung, and B. B. Iversen, *Nat. Commun.* **8**, 13901 (2017).
- [36] J. C. Y. Teo, L. Fu, and C. L. Kane, *Phys. Rev. B* **78**, 045426 (2008).
- [37] H.-J. Zhang, C.-X. Liu, X.-L. Qi, X.-Y. Deng, X. Dai, S.-C. Zhang, and Z. Fang, *Phys. Rev. B* **80**, 085307 (2009).
- [38] X.-G. Zhu and P. Hofmann, *Phys. Rev. B* **89**, 125402 (2014).